

Enhanced Valley Zeeman Splitting in Fe-Doped Monolayer

MoS₂

Qi Li^{1,8}, Xiaoxu Zhao^{2,8}, Longjiang Deng¹, Zhongtai Shi¹, Sheng Liu⁴, Qilin Wei⁵,
Linbo Zhang¹, Yingchun Cheng^{5*}, Li Zhang¹, Haipeng Lu¹, Weibo Gao⁴, Wei Huang⁵,
Cheng-Wei Qiu⁷, Gang Xiang⁶, Stephen John Pennycook², Qihua Xiong⁴, Kian Ping
Loh^{3*} and Bo Peng^{1*}

¹National Engineering Research Center of Electromagnetic Radiation Control
Materials, School of Electronic Science and Engineering, University of Electronic
Science and Technology of China, Chengdu, 611731, China

²Department of Materials Science and Engineering, National University of Singapore,
9 Engineering Drive 1, 117575, Singapore

³Department of Chemistry and Centre for Advanced 2D Materials and Graphene
Research Centre, National University of Singapore, 117549, Singapore

⁴Division of Physics and Applied Physics, School of Physical and Mathematical
Sciences, Nanyang Technological University, 637371, Singapore

⁵Key Laboratory of Flexible Electronics & Institute of Advanced Materials, Nanjing
Tech University, Nanjing, 211816, China

⁶College of Physical Science and Technology, Sichuan University, Chengdu, 610064,
China

⁷Department of Electrical and Computer Engineering, National University of
Singapore, 117583, Singapore

⁸Qi Li and Xiaoxu Zhao contributed equally to this work.

*Correspondence to bo_peng@uestc.edu.cn (B.P.), iamyccheng@njtech.edu.cn
(YC.C), chmlhkp@nus.edu.sg (K.P.L)

Abstract: The “Zeeman effect” offers unique opportunities for magnetic manipulation of the spin degree of freedom (DOF). Recently, valley Zeeman splitting, referring to the lifting of valley degeneracy, has been demonstrated in two-dimensional transition metal dichalcogenides (TMDs) at liquid helium temperature. However, to realize the practical applications of valley pseudospins, the valley DOF must be controllable by a magnetic field at room temperature, which remains a significant challenge. Magnetic doping in TMDs can enhance the Zeeman splitting, however, to achieve this experimentally is not easy. Here, we report unambiguous magnetic manipulation of valley Zeeman splitting at 300 K ($g_{eff} = -6.4$) and 10 K ($g_{eff} = -11$) in a CVD-grown Fe-doped MoS₂ monolayer; the effective Landé g_{eff} factor can be tuned to -20.7 by increasing the Fe dopant concentration, which represents an approximately fivefold enhancement as compared to undoped MoS₂. Our measurements and calculations reveal that the enhanced splitting and g_{eff} factors are due to the Heisenberg exchange interaction of the localized magnetic moments (Fe 3*d* electrons) with MoS₂ through the *d*-orbital hybridization.

Keywords: magnetic doping, valleytronic, spin, ferromagnetic, 2D transition metal dichalcogenides

Room-temperature manipulation of the spin degree of freedom (DOF) is crucial for spintronic and valleytronic devices.^{1, 2} Two-dimensional transition metal dichalcogenides (TMDs) exhibit a distinguishable carrier distribution in two momentum-dependent valleys;³⁻⁷ the broken spatial inversion symmetry together with the strong spin-orbit coupling (SOC) results in the coupling of the spin and valley, giving rise to valley-dependent optical selection rules.⁸ The spin-up (-down) holes and spin-down (-up) electrons mostly exist in the $+K$ ($-K$) momentum valley under optical pumping by the right-handed σ^+ (left-handed σ^-) polarized light. The spin and valley ($+K$ and $-K$) information can be optically detected with polarization-resolved photoluminescence (PL). The chiral optical selection rules allow that valley Zeeman splitting (ΔE) can be read-out optically,⁹ which is defined as the energy difference between the opposite circularly polarized PL, $\Delta E = E(\sigma^-) - E(\sigma^+) = 2(\Delta_L + \Delta_V + \Delta_S)$. The total cumulative magnetic moment μ consists of atomic orbital magnetic moment $\mu_L (m\mu_B)$, valley magnetic moment $\mu_V (\Delta\alpha\tau\mu_B)$ and spin magnetic moment $\mu_S (\mu_B)$, where $\tau = \pm 1$ represents the index for the $\pm K$ valleys, m is the magnetic quantum number of d -orbitals, $\Delta\alpha$ is the difference in the valley g -factors of the conduction and valence bands, and μ_B is the Bohr magneton.⁵ The interaction of the magnetic moment μ with a magnetic field B can lift the valley degeneracy and slightly shift the energy of the valence and conduction bands in the two valleys, resulting in the splitting of the PL spectrum lines of the $+K$ and $-K$ valleys, analogous to the “Zeeman effect”. Zeeman-type valley splitting has been studied in monolayer WSe_2 ,^{4, 5, 10} monolayer MoS_2 and WS_2 ,^{11, 12} monolayer MoSe_2 ,^{3, 13} and bilayer MoTe_2 ¹⁴ under an out-of-plane

magnetic field. The interfacial magnetic exchange field has also been utilized to enhance the Zeeman-type valley splitting in a heterojunction geometry comprising monolayer TMDs and magnetic films (EuS, CrI₃).^{15, 16}

Increasing the valley Zeeman splitting is of great importance for valley polarization control for logic applications.¹⁷ A 15 meV valley Zeeman splitting was observed using an extremely high magnetic field up to 65 T at 4 K.¹¹ Considerable efforts have also been devoted to enlarging the effective Landé g_{eff} factor, which is estimated to be approximately -4 in pristine monolayer TMDs.^{3, 10, 15, 18} Recently, the g_{eff} factor was observed to be as high as -18 by increasing the electron density in heavily gated monolayer TMDs, which originates from the exciton-polaron resonance and phase-space filling effect.¹⁹⁻²² In the field of magnetically doped semiconductors, J. K. Furdyna and H. Ohno have done pioneering researches and brought diluted magnetic semiconductor (DMS) to prominence on the world scale.²³⁻²⁵ The presence of magnetic ions results in the $sp-d$ exchange interaction between the band electrons and the localized magnetic moments,²⁶⁻²⁸ which further leads to extremely large Zeeman splitting and ferromagnetism.²⁹⁻³¹ Theoretically, magnetic doping in monolayer TMDs has been predicted to increase the magnetic susceptibility, even possibly giving rise to magnetic order and rich physics due to the interaction between the SOC and local ferromagnetism.^{32, 33} However, substitutional doping of monolayer TMDs without collateral damage to the lattice is currently very challenging.

In this work, we observed enhanced valley Zeeman splitting in CVD-grown Fe-doped monolayer MoS₂ by circularly polarized magneto-photoluminescence, with

a g_{eff} factor of -6.4 at 300 K. The g_{eff} factor exponentially increases to approximately -11 as the temperature decreases to 10 K and is further monotonically tuned to -20.7 by increasing the Fe dopant concentration. This value corresponds to an approximately fivefold enhancement as compared to undoped monolayer MoS₂. Using first-principles calculations, we propose that the enhanced valley Zeeman splitting and g_{eff} factor are attributed to the isotropic Heisenberg exchange interaction of magnetic moments arising from the d -orbital hybridization of Fe and Mo atoms.

Results and discussion

Structure and phase of Fe-doped monolayer MoS₂. Fe-doped monolayer MoS₂ was grown on Si/SiO₂ substrates by the CVD method (see Methods and Fig. 1a-d). The layer identification was corroborated by direct topography measurements with an atomic force microscope (AFM). The 0.9-nm step height exactly corresponds to the thickness of CVD-grown monolayer MoS₂^{34, 35} (see Supplementary Information Fig. S1). The in-plane E_{2g}¹ vibration mode and out-of-plane A_{1g} vibration mode of CVD-grown monolayer MoS₂ (P1) are at ~380.8 and ~401.6 cm⁻¹, respectively (Fig. 1e); the energy difference between the A_{1g} and E_{2g}¹ modes is ~20.8 cm⁻¹, which is consistent with the fingerprint of monolayer MoS₂ grown by the CVD method.^{36, 37} The Fe atom substitutions induce stiffening of the E_{2g}¹ mode and softening of the A_{1g} mode, resulting in E_{2g}¹ (A_{1g}) shifting to higher (lower) frequency; however, the defects in MoS₂ can lead to broadening and an opposite shifts of the E_{2g}¹ and A_{1g} Raman peaks.³⁸ Thus, the shifts of the A_{1g} and E_{2g}¹ peaks depend on competing effects by substitutions and disorder in the CVD-grown Fe-doped monolayer MoS₂. Two

pronounced exciton emission features at ~ 1.82 and ~ 1.95 eV are clearly observed at room temperature, which are associated with the A and B excitons of monolayer MoS₂.^{8, 39} The Fe dopants introduce an additional nonradiative recombination way, resulting in an increasing nonradiative decay rate, thus the PL intensity decreases as the Fe dopant concentrations increase (Fig. 1f).⁴⁰

To validate the substitution of Mo by Fe atoms (Fe_{Mo}), we investigated the structure and phase of the CVD-grown Fe-doped MoS₂ monolayer on an atomic scale by employing an aberration-corrected scanning transmission electron microscope with an annular dark field detector (STEM-ADF) operated at a low accelerating voltage (60 kV). The maximum energy from 60 kV electron beam is smaller than the threshold to damage of MoS₂. The STEM-ADF image represents the inherent elastically scattered electrons; therefore, the image contrast of the ADF image depends on the atomic number Z , varying as approximately $Z^{1.6-1.7}$. This phenomenon renders STEM-ADF imaging a powerful tool to unveil the atomic structures of 2D materials.⁴¹ The presence of substitutional doping of Mo by Fe is reflected by the contrast reduction in the STEM-ADF image (Fig. 2a and Supplementary Information Fig. S2). The location and density of Fe dopants were calculated based on the contrast reduction, and the mapping of all atom species of the Fe-doped MoS₂ monolayer is depicted in Fig. 2b. Statistical sampling shows that the concentration of Fe substitutes is $\sim 2\%$ based on statistical analysis, suggesting a Mo_{0.98}Fe_{0.02}S₂ chemical stoichiometry. The contrast of the Fe atom is approximately equal to that of the S dimer (Fig. 2c), which is confirmed by the corresponding simulated image (Fig. 2d-e). Furthermore, the

presence of the Fe dopant is verified by the electron energy loss spectrum (EELs) (Fig. 2f and Supplementary Information Fig. S3); the sharp Fe L-edge features are clearly detected. The presence of Fe dopants (Fig. 2g) does not impact the structural integrity of monolayer MoS₂. Neither additional S vacancies nor discernible strain (Fig. 2h) proximal to the Fe dopant site are introduced into the pristine lattices. Therefore, the Fe dopants do not damage the lattice of the MoS₂ monolayer, which is attributed to the nearly equal ionic radius between Fe and Mo ions.

Valley Zeeman splitting in Fe-doped monolayer MoS₂. The valley Zeeman splitting in pristine MoS₂ is attributed to the valley magnetic moment and the atomic orbital magnetic moment of the Mo *d*-orbital.⁵ However, the introduction of Fe atoms leads to the *d*-orbital hybridization of Fe and Mo atoms, which significantly enhance the valley Zeeman splitting (Fig. 3a). The measurements of polarization-resolved PL spectra under an out-of-plane magnetic field were performed on the Fe-doped monolayer MoS₂ using a confocal Raman/PL microscope system, which was checked by polarization-resolved Si Raman spectra obtained under excitation by circularly polarized light at 2.41 and 1.96 eV. The helicity parameters of Si Raman feature are up to 98% and 93%, respectively, verifying that our optical system is excellently calibrated (Supplementary Information Fig. S4). Figure 3b-d shows the normalized polarization-resolved PL spectra of the neutral A exciton of the Fe-doped MoS₂ monolayer (P1) at selected values of the magnetic field at 10 K. At 0 T, the σ^- circular polarization PL emission from the $-K$ valley (red curve) is completely identical to the σ^+ PL emission from the $+K$ valley (blue curve). However, at high field, the σ^- and σ^+

PL peaks split due to the time-reversal symmetry breaking; the σ^- (σ^+) PL peak shifts to a higher energy than σ^+ (σ^-) at -7 T (+7 T), indicating the occurrence of valley Zeeman splitting. The long-range magnetic orders are forbidden in the Fe-doped MoS₂ monolayer at 10 K (see Supplementary Information Fig. S5), thus, the Fe-doped MoS₂ monolayer is not ferromagnetic and no valley Zeeman splitting is observed at zero external fields. Valley Zeeman splitting is revealed more clearly through the intensity difference (ΔPL) in the normalized polarization-resolved PL at ± 7 T and 0 T (Fig. 3e), $\Delta PL = I(\sigma^-) - I(\sigma^+)$. At zero field (black curve), ΔPL is almost equal to zero. In contrast, at ± 7 T, ΔPL deviates from zero and displays opposite values symmetric about 0 T when the direction of the magnetic field is switched, with a positive (negative) value for +7 T (-7 T) below ~ 1.88 eV and an inverse trend above this value. This observation implies that, whereas the magnitude depends on the magnetic field intensity, the sign of valley splitting is determined by the relationship between the helicity and the magnetic field direction. Importantly, valley Zeeman splitting is extracted by computing the “center of mass” of the PL peak. The splitting as a function of B is shown in Fig. 3f, yielding a g_{eff} factor of -11 ± 0.5 . The linear magnetic-field-dependence of valley Zeeman splitting in Fe-doped monolayer MoS₂ arises from the linear variation of intrinsic Zeeman splitting ($g\mu_B B$) and localized Fe spins ($\langle S \rangle$) with magnetic field.^{25, 42}

To further verify the increasing effective g_{eff} factor in Fe-doped monolayer MoS₂, exfoliated and undoped CVD-grown MoS₂ monolayers were used as control samples and measured at 10 K in the same polarization-resolved optical system

(Supplementary Information Fig. S6). The g_{eff} factors of the exfoliated and undoped CVD-grown MoS₂ monolayers are -4.4 ± 0.5 and -4.5 ± 0.5 at 10 K, respectively. Thus, the g_{eff} factors of Fe-doped monolayer MoS₂ are at least $\sim 250\%$ times larger than that of exfoliated and undoped CVD-grown MoS₂ monolayer (Fig. 3f and 3g). The valley Zeeman splitting can be strikingly tuned by controlling the Fe dopant concentration, which significantly increases as the Fe dopant concentration increases. The g_{eff} factor of Fe-doped MoS₂ monolayer achieves a maximum of approximately -20.7 ± 1.0 , which is ~ 5 times as larger as that of exfoliated and undoped CVD-grown MoS₂ (Fig. 3g and Supplementary Information Fig. S6 and S7).

The absorption spectra of all samples were examined at 10 K (see Supplementary Information Fig. S8a-b). Only excitons A and B are observed, and no distinguishable trion absorption peak due to electron doping is detected.⁸ Therefore, the possibility of electron doping leading to the increase in g_{eff} factor is ruled out.^{8, 18, 19, 43} We also measured Zeeman-type spin splitting of defect emission in monolayer MoS₂ (see Supplementary Information Fig. S8c-f). Strikingly, the g_{eff} factor of defect emission is approximately -6.0 at 10 K, which is only half and even $1/4$ of that in Fe-doped MoS₂ monolayer (Fig. 3). Thus, the enhancements of g_{eff} factor in Fe-doped MoS₂ monolayer are not induced by defects. The Fe dopants are anticipated to lead to the distinct increase in g_{eff} factor and valley Zeeman splitting.

Importantly, unambiguous valley Zeeman splitting is observed at room temperature, although it is smaller than the PL linewidth. At zero field, the σ^- and σ^+ PL spectra from the $-K$ and $+K$ valleys are completely overlapped; however, they split at high

field, with inverse shifting directions for +7 T and -7 T (P2, see Supplementary Information Fig. S9). The spectral line shape of ΔPL at room temperature is consistent with that at 10 K, whereas the ΔPL intensity decreases by 50%. Thus, ΔPL clearly shows the occurrence of valley Zeeman splitting at room temperature, which follows a linear relation with B , giving a g_{eff} factor of -6.4 ± 0.5 at 300 K (see Supplementary Information Fig. S9a and S9d), which is ~ 1.6 times as large as that of undoped CVD-grown monolayer MoS_2 with a g_{eff} factor of -3.9 at 300 K (see Supplementary Information Fig. S9b and S9d); the g_{eff} factor of Fe-doped MoS_2 monolayer also increases with increasing Fe dopant concentration at room temperature, achieving a maximum of approximately -15.7 , which represents an enhancement of $\sim 400\%$ as compared to CVD-grown undoped monolayer MoS_2 (see Supplementary Information Fig. S9e). Thus, spin manipulation in TMDs can be pushed to room temperature from liquid He temperature limit.

To further understand the valley Zeeman splitting, the temperature dependence of the valley Zeeman splitting and g_{eff} factor were determined on Fe-doped monolayer MoS_2 . Figure 4a-b shows the polarization-resolved PL spectra as a function of temperature at -7 T and +7 T. The valley Zeeman splitting between the σ^- and σ^+ PL components is distinct, whereas the splitting increases as the temperature decreases from 300 K to 10 K (P1, Fig. 4a-c). Figure 4c shows the valley Zeeman splitting extracted from Fig. 4a-b as a function of temperature at ± 7 T, indicating a monotonic increase in the splitting with decreasing temperature. Figure 4d shows the temperature dependence of the effective g_{eff} factor of Fe-doped MoS_2 monolayer, which increases

by nearly 1 times as the temperature decreases from 300 K to 10 K; in contrast, the g_{eff} factor of undoped CVD-grown MoS₂ monolayer almost keep constant and slightly change from -3.9 to -4.5 with the decreasing temperature from 300 K to 10 K (see Supplementary Information Fig. S9d and S6d).

Heisenberg exchange interaction mechanism for valley Zeeman splitting. The enhancement of valley Zeeman splitting and g_{eff} factor in Fe-doped monolayer MoS₂ can be explained by the kp mode using the effective Hamiltonian for the $+K$ and $-K$ valleys. In undoped monolayer MoS₂, the spin splitting in the valleys originates from the inversion symmetry breaking together with the SOC, which are opposite in different valleys due to time-reversal symmetry (Fig. 5a). The total Hamiltonian is expressed as $H(k) = at(\tau k_x \sigma_x + k_y \sigma_y) + \Delta \sigma_z / 2 - \lambda \tau (\sigma_z - 1) s_z / 2$, where a , t , Δ , and τ represent the lattice constant, effective hopping integral, energy gap and valley index, respectively, 2λ is the spin splitting at the top of the valence band due to the SOC, and s_z is the Pauli matrix for spin.⁴⁴⁻⁴⁶ The last term in $H(k)$ is the SOC term causing valence band splitting. In the presence of Fe dopant, an additional Heisenberg exchange Hamiltonian term $H_m = -xJ_{eff} \langle S \rangle s_z$ that modifies the valley spin polarization of Fe-doped monolayer MoS₂ is introduced, where x and J_{eff} are the dopant concentration, the exchange constant, respectively. $\langle S \rangle$ is the magnetic-field-dependent localized Fe spins along the magnetic field. Thus, the spin splitting at the top of the valence band of the $+K$ and $-K$ valleys should be expressed as $2\lambda + (2\Delta E_{Fe} + g\mu_B B) / 2$ and $2\lambda - (2\Delta E_{Fe} + g\mu_B B) / 2$ (Fig. 3a), respectively, where $2\Delta E = xJ_{eff} \langle S \rangle$. Therefore, valley Zeeman splitting is expressed as

$\Delta E = g\mu_B B + xJ_{eff} \langle S \rangle$. The Fe dopants result in enhanced valley Zeeman splitting, which increases with increasing dopant concentration. Importantly, previous works have reported that the localized Fe spins $\langle S \rangle$ show a linear variation with magnetic field,^{25, 42, 47} which drastically contrasts with the nonlinear dependence of Mn spins in Mn-doped diluted magnetic materials ($\text{Hg}_{1-x}\text{Mn}_x\text{Te}$, $\text{Cd}_{1-x}\text{Mn}_x\text{Se}$, $\text{Cd}_{1-x}\text{Mn}_x\text{Te}$).^{28, 29} Therefore, valley Zeeman splitting of monolayer Fe-doped MoS_2 is linearly dependent with magnetic field, consistent with the above experimental results, as shown in Fig. 3 and Supplementary Information Fig. S7.

Finally, we briefly discuss the temperature dependence of valley Zeeman splitting and the g_{eff} factor. In the Heisenberg exchange interaction mode, the exchange constant J_{eff} is a sensitive function of the interatomic distance,⁴⁸ expressed as $J_{eff} = J_0 \exp(-\chi \langle r \rangle_T)$, where $\langle r \rangle_T$ represents the displacement of the equilibrium separation between Mo and Fe atoms from absolute zero ($\langle r \rangle_0 = 0$), which originates from lattice thermal expansion and displays a positive linear dependence with temperature in MoS_2 materials,^{49, 50} $\langle r \rangle_T = \alpha T$. Magnetic order is strongly suppressed by thermal fluctuations in the monolayer Fe-doped MoS_2 according to the Mermin-Wagner theorem. Therefore, the temperature dependence of the localized spins originating from Fe atoms is predicted by the Boltzmann distribution ($\exp(-\Delta / k_B T)$) rather than the Brillouin law used in traditional three-dimensional diluted magnetic semiconductor,^{42, 51, 52} where Δ is the energy barriers of Fe spin flipping. Therefore, the valley Zeeman splitting increases with decreasing temperature, leading to an increase in the g_{eff} factor, in agreement with our

experimental results (see the solid line in Fig. 4c and 4d). The energy barrier of Fe spin flipping is estimated to be $\sim 10^{-4}$ meV, indicating that the spin flipping is suppressed only below ~ 1 mK ($k_B T$), thus, the long-range magnetic order is strongly prohibited and no ferromagnetism is observed in Fe-doped MoS₂ monolayer at 10 K (see Supplementary Information Fig. S5), which is consistent with the experimental result of no valley Zeeman splitting at 0 T (Fig. 3c). The lattice thermal expansion dominates the temperature dependence of valley Zeeman splitting and the g_{eff} factor.

Further insights into the origin of the enhanced valley Zeeman splitting can be obtained from the calculated electronic band structures of undoped monolayer MoS₂ and Fe-doped monolayer MoS₂ (Fig. 5). The calculations show that the formation energy of Fe_{Mo} is lowest in S-rich condition, indicating that the Fe_{Mo} substitutions are favorable (see Supplementary Information Section 10), consistent with our experiments (Fig. 2 and Supplementary Information Fig. S2 and S3). Strikingly, the valley spin states in Fe-doped monolayer MoS₂ are different from those in undoped pristine MoS₂ monolayer (Fig. 5a-b). Valley Zeeman splitting is clearly observed at and in the vicinity of *K* points in Fe-doped MoS₂ monolayer, while there is no any valley splitting in undoped MoS₂ monolayer⁴⁶. Figure 5c-e shows the calculated electronic band structures of orbitals of Mo, Fe and S atoms in Fe-doped monolayer MoS₂, demonstrating that the states in the valence band of Fe-doped monolayer MoS₂ are formed primarily from the *d*-orbitals of Mo and Fe and *p*-orbitals of S. The components of the Fe *d*-orbital are distinct in the electronic band structures, although the *d*-orbital of Mo and *p*-orbitals of S predominates. Figure 5f shows the

corresponding orbital percentage of d_{z^2} , $d_{x^2-y^2}$ and d_{xy} at the valence band maximum (VBM) and conduction band minimum (CBM) in the $+K$ valley, which dominate the valley Zeeman splitting. The d -orbital ratios of Fe to Mo atoms are up to $\sim 1\%$ and $\sim 10\%$ at the CBM and VBM points, respectively, strikingly validating the occurrence of d -orbital hybridization of Fe and Mo atoms. The VBM of the Fe-doped MoS_2 is mainly composed of the $d_{x^2-y^2}$ and d_{xy} orbitals of Mo and Fe atoms with $m = \pm 2$ in $\pm K$ valley (Fig. 5f-g), while the CBM consists of d_{z^2} orbitals of Mo and Fe atoms with $m = 0$.⁵³ The density of states (DOS) also verify that the d -orbitals of Fe atoms contribute to the orbital hybridization (see Supplementary Information Fig. S11a). Therefore, the Heisenberg exchange interaction of magnetic dopant Fe atoms and MoS_2 arises from the hybridization of the d -orbitals of Mo and Fe, leading to the enhanced valley Zeeman splitting. In our first-principles calculations, the 4×4 (Fig. S10) and 5×5 (Fig. 5 and Fig. S11) supercells with one Fe atom replacing one Mo atom were used. The local magnetic moments originating from Fe atoms are ordered at 0 K, analogous to that under a strong external magnetic field. However, the induced effective magnetic field may be much stronger than our applied magnetic field; moreover, the maximum concentration of Fe dopant is only 2% in our experiments, which is much smaller than the doping concentration ($\sim 7\%$) in calculations. Thus, the deviation between the calculated and experimental values of valley Zeeman splitting is reasonable. Nonetheless, the calculated trends are consistent with our experimental observations in supporting the enhanced valley Zeeman splitting in Fe-doped MoS_2 .

Conclusion

In summary, we have demonstrated an enhanced g_{eff} factor and valley Zeeman splitting in Fe-doped monolayer MoS₂, arising from the Heisenberg exchange interaction between the local magnetic moments and MoS₂ through the d -orbital hybridization. This result could potentially give rise to many interesting phenomena such as the tunneling magnetic-resistance effect and spin Hall effect.⁵⁴⁻⁵⁶ Our proposed approach for magnetic doping and manipulation of valley spin at room temperature is not limited to MoS₂ and can be achieved in a variety of TMDs, including WSe₂, MoSe₂ and WS₂. These features highlight the potential to synthesize magnetic 2D materials and to produce quantum confined spintronic and valleytronic devices at room temperature.^{57, 58}

Experimental methods

Synthesis of Fe-doped MoS₂ monolayer: MoO₃ (15 mg) and FeS₂ (99.99%, Aldrich) were mixed at a molar ratio of Fe to Mo of 0.12, 0.24, 0.48 and 0.4 and placed in a quartz boat inside a quartz tube at the center of a heating zone. A clean SiO₂/Si substrate (285 nm SiO₂) was treated with PTCA solution (5% wt) and placed in the downstream region. The quartz tube was first evacuated to a pressure of 20 mTorr, followed by a 50 sccm flow of Ar/H₂ (95%/5%). Sulfur powder (1 g) was placed in a separate quartz boat in the upstream region and heated from room temperature to 290 °C by a heating belt when the MoO₃ temperature was ~500 °C. The Fe-doped MoS₂ monolayer was synthesized by three-step heating process: 20-600 °C for 30 min, 600-760 °C for 40 min, and 760 °C for 15 min. Finally, all heating was stopped and the samples were cooled to room temperature.

Optical Spectroscopy Measurement: The PL and Raman signals were measured by a Witec Alpha 300R confocal Raman microscope system, coupled with a 7 T superconductive magnetic field and a closed cycle optical cryostat (10 K). In the polarization-resolved PL measurement system, a linearly polarized laser beam passes through a $1/4\lambda$ waveplate, and is then focused on the samples by a long working distance objective (Olympus, 50x, NA = 0.45). The circularly polarized PL is collected by the same objective, and passes through the same $1/4\lambda$ waveplate and an analyzer into a spectrometer and a CCD camera (see Supplementary Information Fig. S12). The PL and Raman spectra were collected under a 2.41 eV laser excitation of 3.0 mW. The overlap of MoS₂ and Si Raman features with photoluminescence features can conceal the splitting under nearly on-resonance excitation (1.96 eV), especially at low temperature (10 K) (see Supplementary Information Fig. S13); therefore, the excitation wavelength was detuned to 2.41 eV in our experiments.

STEM Characterization and Image Simulation: Fe-doped monolayer MoS₂ was transferred onto a TEM grid from the SiO₂/Si substrates using the PMMA-assisted method. STEM-ADF imaging was performed by an aberration-corrected JEOL ARM-200F with a cold field emission gun and an ASCOR probe corrector at 60 kV. The convergence semiangle of the probe was ≈ 30 mrad. STEM-ADF images were collected using a half-angle range from ≈ 85 to 280 mrad. Dwell times of 19 and 10 $\mu\text{s pixel}^{-1}$ were set for single-scan imaging and sequential imaging, respectively. The QSTEM package was used for image simulations by assuming an aberration-free probe and an ≈ 1 Å source size to give a probe size of ≈ 1.2 Å.

Associated content

Supporting Information

The authors declare no competing financial interest.

The Supporting Information is available free of charge on the ACS Publications website

1. Thickness of Fe-doped monolayer MoS₂.
2. Large-area atomic-resolution STEM-ADF image of CVD-grown Fe-doped monolayer MoS₂.
3. EELs mapping of CVD-grown Fe-doped monolayer MoS₂.
4. Optical system calibration by polarization-resolved Si Raman spectra.
5. Reflective magnetic circular dichroism measurement (RMCD).
6. Control experiments in undoped MoS₂ monolayer.
7. Valley Zeeman splitting increase with increasing Fe dopant concentration.
8. Excluding the possibility of carrier doping and defects for g_{eff} factor enhancement in Fe-doped monolayer MoS₂.
9. Room-temperature valley Zeeman splitting in Fe-doped monolayer MoS₂.
10. Calculation details and results of Fe-doped monolayer MoS₂.
11. The density of states (DOS) of Fe-doped MoS₂ monolayer calculated from a 5x5x1 MoS₂ supercell with one Fe atom substituting one Mo atom.
12. Confocal polarization-resolved PL/Raman microscope system.
13. Valley polarization in Fe-doped monolayer MoS₂ upon on-resonance excitation.

Corresponding Author

- * Bo Peng: bo_peng@uestc.edu.cn
- * Kian Ping Loh: chmlhkp@nus.edu.sg
- * Yingchun Cheng: iamyccheng@njtech.edu.cn

ORCID

Bo Peng: 0000-0001-9411-716X

Kian Ping Loh: 0000-0002-1491-743X

Author Contributions

B.P. and L.J.D developed the concept, designed the experiment and prepared the manuscript. Q.L, S.Z.T. performed the polarization-resolved PL measurements. X.X.Z, K.P.L and S.J.P contributed to the measurement of STEM-ADF. M.J.Z, L.B.Z synthesized the monolayer Fe-doped MoS₂. S.L., Q.H.X contributed to the study of AFM. Y.C.C., Q.L.W., W.H. contributed to fully relativistic calculations. B.P, W.B.G., L.Z., H.P.L., C.W. Q., and G.X. contributed to the study of mechanism.

Acknowledgments

We acknowledge financial support from National Science Foundation of China (51602040, 51872039), Science and Technology Program of Sichuan (M112018JY0025) and Scientific Research Foundation for New Teachers of UESTC (A03013023601007). We thank Prof. Jianhua Zhao and Dr. Hailong Wang from Institute of Semiconductors, Chinese Academy of Sciences for the helpful suggestions on the diluted magnetic semiconductor.

References

1. Tombros, N.; Jozsa, C.; Popinciuc, M.; Jonkman, H. T.; van Wees, B. J. Electronic Spin Transport and Spin Precession in Single Graphene Layers at Room

Temperature. *Nature* **2007**, *448*, 571-574.

2. Bonilla, M.; Kolekar, S.; Ma, Y.; Diaz, H. C.; Kalappattil, V.; Das, R.; Eggers, T.; Gutierrez, H. R.; Phan, M.-H.; Batzill, M. Strong Room-Temperature Ferromagnetism in VSe₂ Monolayers on van der Waals Substrates. *Nat. Nanotechnol.* **2018**, *13*, 289-293.
3. MacNeill, D.; Heikes, C.; Mak, K. F.; Anderson, Z.; Kormányos, A.; Zólyomi, V.; Park, J.; Ralph, D. C. Breaking of Valley Degeneracy by Magnetic Field in Monolayer MoSe₂. *Phys. Rev. Lett.* **2015**, *114*, 037401.
4. Yuan, H.; Bahramy, M. S.; Morimoto, K.; Wu, S.; Nomura, K.; Yang, B.-J.; Shimotani, H.; Suzuki, R.; Toh, M.; Kloc, C.; Xu, X.; Arita, R.; Nagaosa, N.; Iwasa, Y. Zeeman-Type Spin Splitting Controlled by an Electric Field. *Nat. Phys.* **2013**, *9*, 563-569.
5. Aivazian, G.; Gong, Z.; Jones, A. M.; Chu, R.-L.; Yan, J.; Mandrus, D. G.; Zhang, C.; Cobden, D.; Yao, W.; Xu, X. Magnetic Control of Valley Pseudospin in Monolayer WSe₂. *Nat. Phys.* **2015**, *11*, 148-152.
6. Xiao, D.; Liu, G.; Feng, W.; Xu, X.; Yao, W. Coupled Spin and Valley Physics in Monolayers of MoS₂ and Other Group-VI Dichalcogenides. *Phys. Rev. Lett.* **2012**, *108*, 196802.
7. Zeng, H.; Dai, J.; Yao, W.; Xiao, D.; Cui, X. Valley Polarization in MoS₂ Monolayers by Optical Pumping. *Nat. Nanotechnol.* **2012**, *7*, 490-493.
8. Peng, B.; Li, Q.; Liang, X.; Song, P.; Li, J.; He, K.; Fu, D.; Li, Y.; Shen, C.; Wang, H.; Wang, C.; Liu, T.; Zhang, L.; Lu, H.; Wang, X.; Zhao, J.; Xie, J.; Wu, M.; Bi, L.;

- Deng, L., *et al.* Valley Polarization of Trions and Magnetoresistance in Heterostructures of MoS₂ and Yttrium Iron Garnet. *ACS Nano* **2017**, *11*, 12257-12265.
9. Xu, X.; Yao, W.; Xiao, D.; Heinz, T. F. Spin and Pseudospins in Layered Transition Metal Dichalcogenides. *Nat. Phys.* **2014**, *10*, 343-350.
10. Srivastava, A.; Sidler, M.; Allain, A. V.; Lembke, D. S.; Kis, A.; Imamoglu, A. Valley Zeeman Effect in Elementary Optical Excitations of Monolayer WSe₂. *Nat. Phys.* **2015**, *11*, 141-147.
11. Stier, A. V.; McCreary, K. M.; Jonker, B. T.; Kono, J.; Crooker, S. A. Exciton Diamagnetic Shifts and Valley Zeeman Effects in Monolayer WS₂ and MoS₂ to 65 Tesla. *Nat. Commun.* **2016**, *7*, 10643.
12. Wu, Y. J.; Shen, C.; Tan, Q. H.; Shi, J.; Liu, X. F.; Wu, Z. H.; Zhang, J.; Tan, P. H.; Zheng, H. Z. Valley Zeeman Splitting of Monolayer MoS₂ Probed by Low-Field Magnetic Circular Dichroism Spectroscopy at Room Temperature. *Appl. Phys. Lett.* **2018**, *112*, 153105.
13. Li, Y.; Ludwig, J.; Low, T.; Chernikov, A.; Cui, X.; Arefe, G.; Kim, Y. D.; van der Zande, A. M.; Rigosi, A.; Hill, H. M.; Kim, S. H.; Hone, J.; Li, Z.; Smirnov, D.; Heinz, T. F. Valley Splitting and Polarization by the Zeeman Effect in Monolayer MoSe₂. *Phys. Rev. Lett.* **2014**, *113*, 266804.
14. Jiang, C.; Liu, F.; Cuadra, J.; Huang, Z.; Li, K.; Rasmita, A.; Srivastava, A.; Liu, Z.; Gao, W.-B. Zeeman Splitting *via* Spin-Valley-Layer Coupling in Bilayer MoTe₂. *Nat. Commun.* **2017**, *8*, 802.

15. Zhao, C.; Norden, T.; Zhang, P.; Zhao, P.; Cheng, Y.; Sun, F.; Parry, J. P.; Taheri, P.; Wang, J.; Yang, Y.; Scrace, T.; Kang, K.; Yang, S.; Miao, G.-X.; Sabirianov, R.; Kioseoglou, G.; Huang, W.; Petrou, A.; Zeng, H. Enhanced Valley Splitting in Monolayer WSe₂ due to Magnetic Exchange Field. *Nat. Nanotechnol.* **2017**, *12*, 757-762.
16. Zhong, D.; Seyler, K. L.; Linpeng, X.; Cheng, R.; Sivadas, N.; Huang, B.; Schmidgall, E.; Taniguchi, T.; Watanabe, K.; McGuire, M. A.; Yao, W.; Xiao, D.; Fu, K.-M. C.; Xu, X. van der Waals Engineering of Ferromagnetic Semiconductor Heterostructures for Spin and Valleytronics. *Sci. Adv.* **2017**, *3*, e1603113.
17. Ye, Y.; Xiao, J.; Wang, H.; Ye, Z.; Zhu, H.; Zhao, M.; Wang, Y.; Zhao, J.; Yin, X.; Zhang, X. Electrical Generation and Control of the Valley Carriers in a Monolayer Transition Metal Dichalcogenide. *Nat. Nanotechnol.* **2016**, *11*, 598-602.
18. Wang, Z.; Mak, K. F.; Shan, J. Strongly Interaction-Enhanced Valley Magnetic Response in Monolayer WSe₂. *Phys. Rev. Lett.* **2018**, *120*, 066402.
19. Back, P.; Sidler, M.; Cotlet, O.; Srivastava, A.; Takemura, N.; Kroner, M.; Imamoglu, A. Giant Paramagnetism-Induced Valley Polarization of Electrons in Charge-Tunable Monolayer MoSe₂. *Phys. Rev. Lett.* **2017**, *118*, 237404.
20. Sidler, M.; Back, P.; Cotlet, O.; Srivastava, A.; Fink, T.; Kroner, M.; Demler, E.; Imamoglu, A. Fermi Polaron-Polaritons in Charge-Tunable Atomically Thin Semiconductors. *Nat. Phys.* **2016**, *13*, 255.
21. Kang, M.; Jung, S. W.; Shin, W. J.; Sohn, Y.; Ryu, S. H.; Kim, T. K.; Hoesch, M.; Kim, K. S. Holstein Polaron in a Valley-Degenerate Two-Dimensional Semiconductor.

Nat. Mater. **2018**, *17*, 676-680.

22. Gustafsson, M. V.; Yankowitz, M.; Forsythe, C.; Rhodes, D.; Watanabe, K.; Taniguchi, T.; Hone, J.; Zhu, X.; Dean, C. R. Ambipolar Landau Levels and Strong Band-Selective Carrier Interactions in Monolayer WSe₂. *Nat. Mater.* **2018**, *17*, 411-415.

23. Furdyna, J. K. Diluted Magnetic Semiconductors. *J. Appl. Phys.* **1988**, *64*, R29-R64.

24. Furdyna, J. K. Diluted Magnetic Semiconductors: An Interface of Semiconductor Physics and Magnetism (Invited). *J. Appl. Phys.* **1982**, *53*, 7637-7643.

25. Furdyna, J. K., Kossut, J. Diluted Magnetic Semiconductors. In *Semiconductors and Semimetals*; Willardson, R. K., Beer, A. C., Eds.; Academic Press, inc.: London, 1988; pp 252-257.

26. Furdyna, J. K.; Samarth, N. Magnetic Properties of Diluted Magnetic Semiconductors: A Review (Invited). *J. Appl. Phys.* **1987**, *61*, 3526-3531.

27. Beaulac, R.; Archer, P. I.; Liu, X.; Lee, S.; Salley, G. M.; Dobrowolska, M.; Furdyna, J. K.; Gamelin, D. R. Spin-Polarizable Excitonic Luminescence in Colloidal Mn²⁺-Doped CdSe Quantum Dots. *Nano Lett.* **2008**, *8*, 1197-1201.

28. Gaj, J. A., Kossut, J. Introduction to the Physics of Diluted Magnetic Semiconductors. In *Springer Series in Materials Science*; Hull, R., Jagadish, C., Kawazoe, Y., Kruzic, J., Osgood, R. M., Parisi, J., Pohl, U. W., Seong, T.-Y., Uchida, S.-i., Wang, Z.M., Eds.; Springer, Berlin, Heidelberg, 2010.

29. Yu, J. H.; Liu, X.; Kweon, K. E.; Joo, J.; Park, J.; Ko, K.-T.; Lee, D. W.; Shen, S.;

- Tivakornsasithorn, K.; Son, J. S.; Park, J.-H.; Kim, Y.-W.; Hwang, G. S.; Dobrowolska, M.; Furdyna, J. K.; Hyeon, T. Giant Zeeman Splitting in Nucleation-Controlled Doped CdSe:Mn²⁺ Quantum Nanoribbons. *Nat. Mater.* **2009**, *9*, 47.
30. MacDonald, A. H.; Schiffer, P.; Samarth, N. Ferromagnetic Semiconductors: Moving Beyond (Ga,Mn)As. *Nat. Mater.* **2005**, *4*, 195-202.
31. Ohno, H.; Munekata, H.; Penney, T.; von Molnár, S.; Chang, L. L. Magnetotransport Properties of *p*-Type (In,Mn)As Diluted Magnetic III-V Semiconductors. *Phys. Rev. Lett.* **1992**, *68*, 2664-2667.
32. Cheng, Y. C.; Zhu, Z. Y.; Mi, W. B.; Guo, Z. B.; Schwingenschlögl, U. Prediction of Two-Dimensional Diluted Magnetic Semiconductors: Doped Monolayer MoS₂ Systems. *Phys. Rev. B* **2013**, *87*, 100401.
33. Ramasubramaniam, A.; Naveh, D. Mn-Doped Monolayer MoS₂: An Atomically Thin Dilute Magnetic Semiconductor. *Phys. Rev. B* **2013**, *87*, 195201.
34. Gong, Y.; Liu, Z.; Lupini, A. R.; Shi, G.; Lin, J.; Najmaei, S.; Lin, Z.; Elías, A. L.; Berkdemir, A.; You, G.; Terrones, H.; Terrones, M.; Vajtai, R.; Pantelides, S. T.; Pennycook, S. J.; Lou, J.; Zhou, W.; Ajayan, P. M. Band Gap Engineering and Layer-by-Layer Mapping of Selenium-Doped Molybdenum Disulfide. *Nano Lett.* **2013**, 442-449.
35. Huang, J.-K.; Pu, J.; Hsu, C.-L.; Chiu, M.-H.; Juang, Z.-Y.; Chang, Y.-H.; Chang, W.-H.; Iwasa, Y.; Takenobu, T.; Li, L.-J. Large-Area Synthesis of Highly Crystalline WSe₂ Monolayers and Device Applications. *ACS Nano* **2014**, *8*, 923-930.

36. Wang, S.; Wang, X.; Warner, J. H. All Chemical Vapor Deposition Growth of MoS₂: h-BN Vertical van der Waals Heterostructures. *ACS Nano* **2015**, *9*, 5246-5254.
37. Najmaei, S.; Liu, Z.; Zhou, W.; Zou, X.; Shi, G.; Lei, S.; Yakobson, B. I.; Idrobo, J.-C.; Ajayan, P. M.; Lou, J. Vapour Phase Growth and Grain Boundary Structure of Molybdenum Disulphide Atomic Layers. *Nat. Mater.* **2013**, *12*, 754-759.
38. Liu, Y.; Nan, H.; Wu, X.; Pan, W.; Wang, W.; Bai, J.; Zhao, W.; Sun, L.; Wang, X.; Ni, Z. Layer-by-Layer Thinning of MoS₂ by Plasma. *ACS Nano* **2013**, 4202-4209.
39. Christopher, J. W.; Goldberg, B. B.; Swan, A. K. Long Tailed Trions in Monolayer MoS₂: Temperature Dependent Asymmetry and Resulting Red-Shift of Trion Photoluminescence Spectra. *Sci. Rep.* **2017**, *7*, 14062.
40. Peng, B.; Yu, G.; Zhao, Y.; Xu, Q.; Xing, G.; Liu, X.; Fu, D.; Liu, B.; Tan, J. R. S.; Tang, W.; Lu, H.; Xie, J.; Deng, L.; Sum, T. C.; Loh, K. P. Achieving Ultrafast Hole Transfer at the Monolayer MoS₂ and CH₃NH₃PbI₃ Perovskite Interface by Defect Engineering. *ACS Nano* **2016**, *10*, 6383-6391.
41. Zhao, X.; Dan, J.; Chen, J.; Ding, Z.; Zhou, W.; Loh, K. P.; Pennycook, S. J. Atom-by-Atom Fabrication of Monolayer Molybdenum Membranes. *Adv. Mater.* **2018**, *30*, 1707281.
42. Guldner, Y.; Rigaux, C.; Menant, M.; Mullin, D. P.; Furdyna, J. K. Magneto-optical Evidence of Exchange Interactions in Zero-Gap Hg_{1-x}Fe_xTe Mixed Crystals. *Solid State Commun.* **1980**, *33*, 133-136.
43. Mak, K. F.; He, K.; Lee, C.; Lee, G. H.; Hone, J.; Heinz, T. F.; Shan, J. Tightly Bound Trions in Monolayer MoS₂. *Nat. Mater.* **2013**, *12*, 207-211.

44. Xiao, D.; Liu, G.; Feng, W.; Xu, X.; Yao, W. Coupled Spin and Valley Physics in Monolayers of MoS₂ and Other Group-VI Dichalcogenides. *Phys. Rev. Lett.* **2012**, *108*, 196802.
45. Zhang, Q.; Yang, S. A.; Mi, W.; Cheng, Y.; Schwingenschlögl, U. Large Spin-Valley Polarization in Monolayer MoTe₂ on Top of Euo(111). *Adv. Mater.* **2016**, *28*, 959-966.
46. Cheng, Y. C.; Zhang, Q. Y.; Schwingenschlögl, U. Valley Polarization in Magnetically Doped Single-Layer Transition-Metal Dichalcogenides. *Phys. Rev. B* **2014**, *89*, 155429.
47. Serre, H., Bastard, G., Rigaux, C., Mycielski, J., Furdyna, J. K. Physics of Narrow Gap Semiconductors. Infrared Magnetoabsorption in Zero Gap Hg_{1-x}Fe_xTe and Hg_{1-x}Fe_xSe Mixed Crystals. In *Physics of Narrow Gap Semiconductors*; Gornik, E., Heinrich, H., Palmetshofer, L., Eds.; Springer Berlin Heidelberg: 1982; pp 321-325.
48. Bramwell, S. T. Temperature Dependence of the Isotropic Exchange Constant. *J. Phys.: Condens. Matter* **1990**, *2*, 7527.
49. Sevik, C. Assessment on Lattice Thermal Properties of Two-Dimensional Honeycomb Structures: Graphene, h-BN, h-MoS₂ and h-MoSe₂. *Phys. Rev. B* **2014**, *89*, 035422.
50. Murray, R.; Evans, B. The Thermal Expansion of 2H-MoS₂ and 2H-WSe₂ between 10 and 320 K. *J. Appl. Crystallogr.* **1979**, *12*, 312-315.
51. Spalek, J.; Lewicki, A.; Tarnawski, Z.; Furdyna, J. K.; Galazka, R. R.; Obuszko,

- Z. Magnetic Susceptibility of Semimagnetic Semiconductors: The High-Temperature Regime and the Role of Superexchange. *Phys. Rev. B* **1986**, *33*, 3407-3418.
52. Mermin, N. D.; Wagner, H. Absence of Ferromagnetism or Antiferromagnetism in One- or Two-Dimensional Isotropic Heisenberg Models. *Phys. Rev. Lett.* **1966**, *17*, 1133-1136.
53. Kang, J.; Tongay, S.; Zhou, J.; Li, J.; Wu, J. Band Offsets and Heterostructures of Two-Dimensional Semiconductors. *Appl. Phys. Lett.* **2013**, *102*, 012111.
54. Song, T.; Cai, X.; Tu, M. W.-Y.; Zhang, X.; Huang, B.; Wilson, N. P.; Seyler, K. L.; Zhu, L.; Taniguchi, T.; Watanabe, K.; McGuire, M. A.; Cobden, D. H.; Xiao, D.; Yao, W.; Xu, X. Giant Tunneling Magnetoresistance in Spin-Filter van der Waals Heterostructures. *Science* **2018**, *360*, 1214-1218.
55. Deng, Y.; Yu, Y.; Song, Y.; Zhang, J.; Wang, N. Z.; Sun, Z.; Yi, Y.; Wu, Y. Z.; Wu, S.; Zhu, J.; Wang, J.; Chen, X. H.; Zhang, Y. Gate-Tunable Room-Temperature Ferromagnetism in Two-Dimensional Fe₃GeTe₂. *Nature* **2018**, *563*, 94-99.
56. Klein, D. R.; MacNeill, D.; Lado, J. L.; Soriano, D.; Navarro-Moratalla, E.; Watanabe, K.; Taniguchi, T.; Manni, S.; Canfield, P.; Fernández-Rossier, J.; Jarillo-Herrero, P. Probing Magnetism in 2D van der Waals Crystalline Insulators via Electron Tunneling. *Science* **2018**, *360*, 1218-1222.
57. Huang, B.; Clark, G.; Navarro-Moratalla, E.; Klein, D. R.; Cheng, R.; Seyler, K. L.; Zhong, D.; Schmidgall, E.; McGuire, M. A.; Cobden, D. H.; Yao, W.; Xiao, D.; Jarillo-Herrero, P.; Xu, X. Layer-Dependent Ferromagnetism in a van der Waals Crystal Down to the Monolayer Limit. *Nature* **2017**, *546*, 270-273.

58. Gong, C.; Li, L.; Li, Z.; Ji, H.; Stern, A.; Xia, Y.; Cao, T.; Bao, W.; Wang, C.; Wang, Y.; Qiu, Z. Q.; Cava, R. J.; Louie, S. G.; Xia, J.; Zhang, X. Discovery of Intrinsic Ferromagnetism in Two-Dimensional van der Waals Crystals. *Nature* **2017**, *546*, 265–269.

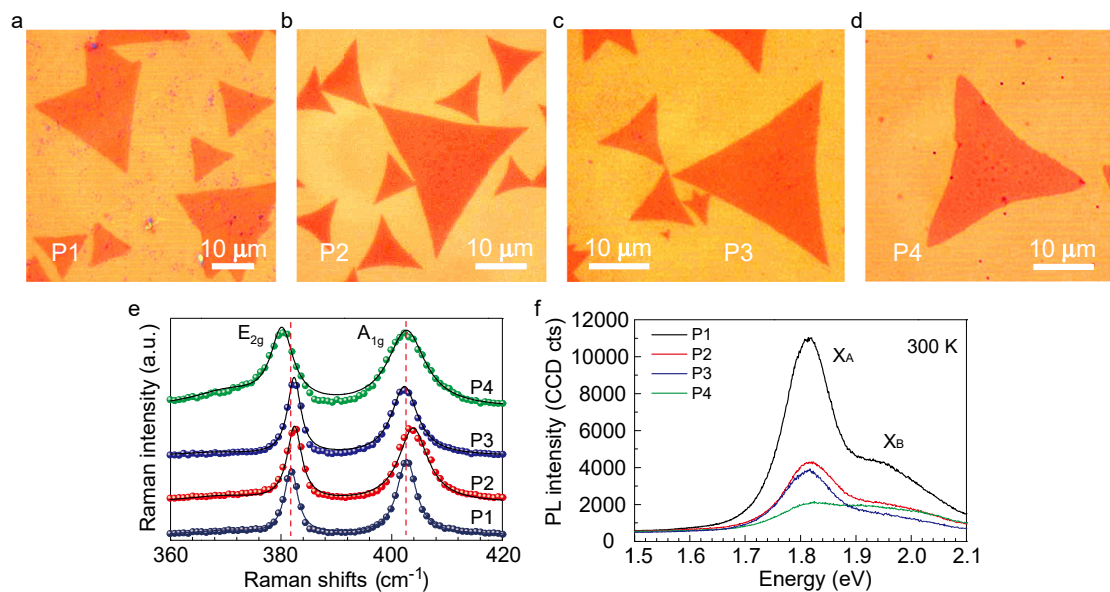


Figure 1. Fe-doped MoS₂ monolayer. (a-d) Optical microscope images of CVD-grown Fe-doped monolayer MoS₂ with the source molar ratio of Fe to Mo of 0.12 (a), 0.24 (b), 0.48 (c) and 0.4 (d). (e-f) Corresponding Raman and photoluminescence spectra of Fe-doped monolayer MoS₂ at room temperature. The PL peaks of A (X_A) and B (X_B) excitons are observed. No trion is induced by the Fe dopants (Fig. S8a-b).

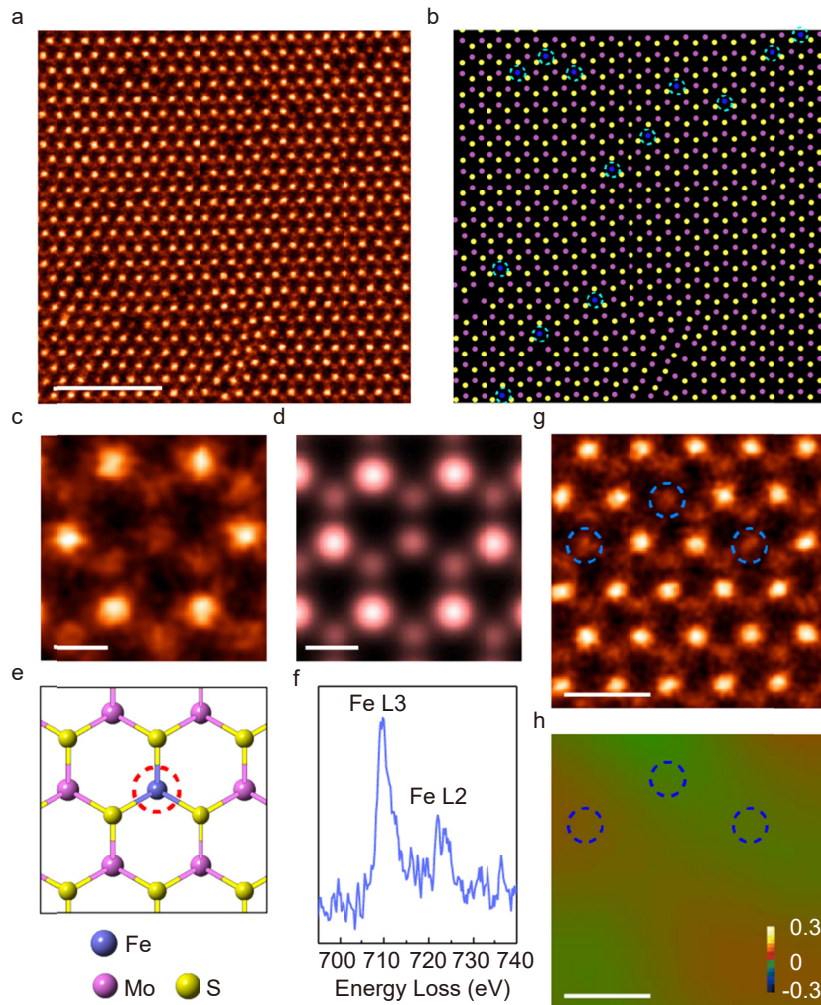


Figure 2. Atomic-resolution STEM-ADF images of Fe-doped MoS₂ monolayer. (a) Typical STEM-ADF image of Fe-doped 1H-MoS₂ monolayer. (b) Corresponding atomic mode of (a) showing the distribution of Fe dopant atoms. Fe, Mo, and S atoms are depicted as blue, pink, and yellow spheres. (c) Enlarged STEM-ADF image revealing a single Fe dopant atom, (d) Corresponding simulated image, and (e) atomic mode. (f) EELs taken from the dopant sites showing a clear Fe L-edge. (g, h) STEM-ADF image (g) containing three Fe dopant atoms (blue dashed circles) and corresponding strain analysis (h), indicating no strain is introduced by Fe dopants. Scale bars: 2 nm in (a), 0.2 nm in (c-d), and 0.5 nm in (g-h).

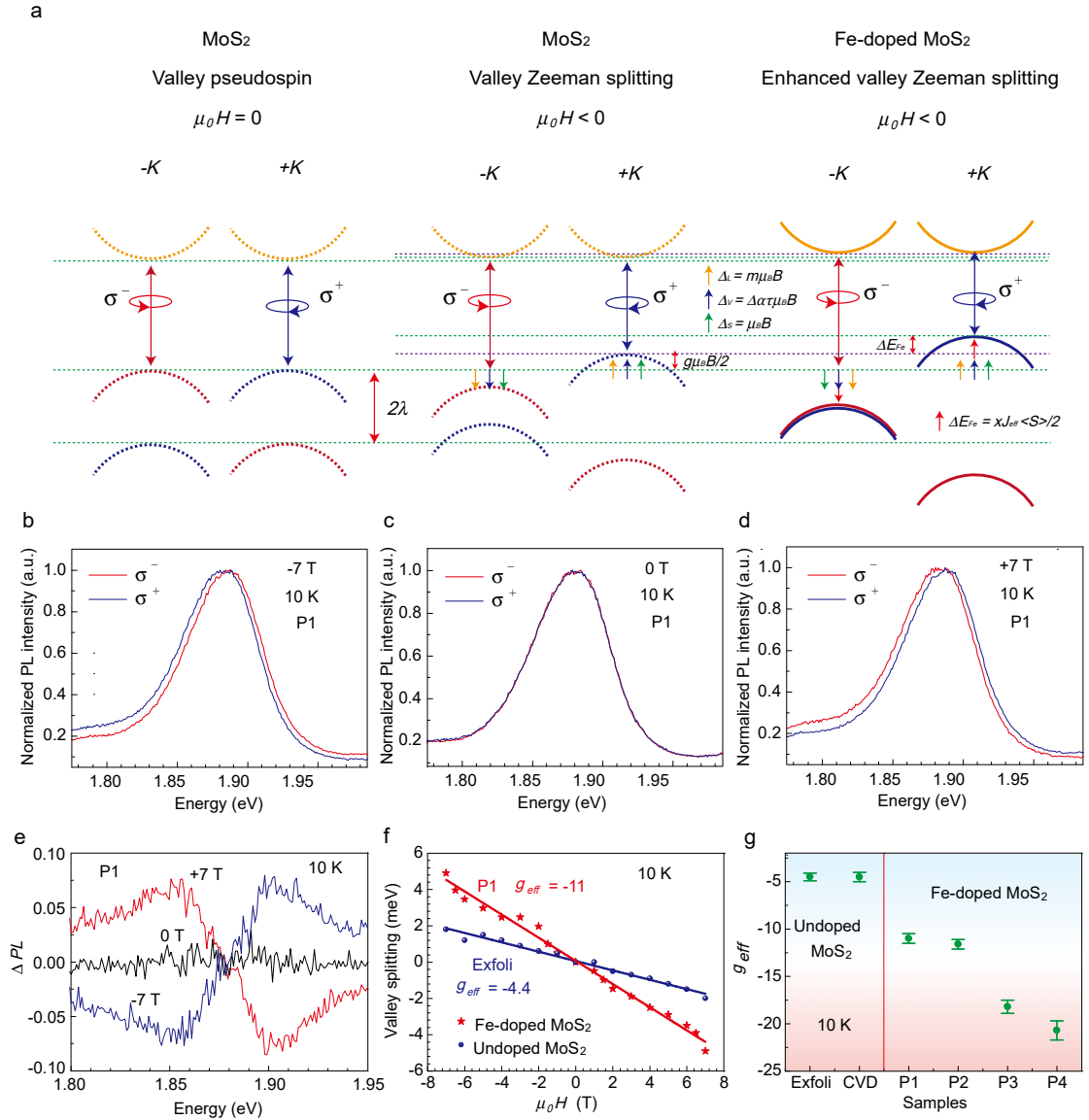


Figure 3. Valley Zeeman splitting. (a) Cartoons illustrating the band structures of the undoped and Fe-doped monolayer MoS₂ near the $\pm K$ points in the absence and presence of a negative magnetic field ($\mu_0 H$, \downarrow). The valance band of pristine MoS₂ monolayer is splitted by 2λ due to SOC (Fig. 3a, left). The external magnetic field lifts the valley degeneracy, leading to valley Zeeman splitting (Fig. 3a, middle). Fe dopant enhances the interaction of the magnetic moment and magnetic field, which gives rise to much more pronounced valley splitting (Fig. 3a, right). (b-d) Normalized raw polarization-resolved valley-exciton PL spectra of Fe-doped monolayer MoS₂ (P1,

Fig. 1a) under magnetic field of 0 and ± 7 T at 10 K. The PL spectra from the $+K$ and $-K$ valleys are completely overlapped at 0 T, but they split at $+7$ T and -7 T, and the PL energy shifts are opposite. To clearly demonstrate the splitting, only PL peaks of A exciton are shown. (e) Difference between the normalized raw σ^- and σ^+ PL components at 0 and ± 7 T, which display no difference at 0 T but obvious opposite trends at ± 7 T, manifesting the occurrence of valley Zeeman splitting. (f) Valley splitting as a function of magnetic field in undoped MoS₂ (exfoliated) and Fe-doped MoS₂ (P1) monolayers at 10 K. The localized Fe spins ($\langle S \rangle$) and intrinsic Zeeman splitting ($g\mu_B B$) are linearly dependent with magnetic field (Ref. 25, 42 and 47), thus valley Zeeman splitting of Fe-doped monolayer MoS₂ follow a linear variation as a function of magnetic field. (g) g_{eff} factor in various of undoped and Fe-doped MoS₂ monolayers. The g_{eff} factors are clearly larger in the Fe-doped MoS₂ monolayer than that in the undoped MoS₂ monolayer; and increase with increasing Fe dopant concentration. All the g_{eff} factors are calculated based on the magnetic-field dependence of valley splitting obtained through “center of mass peak analysis” (Ref. 5).

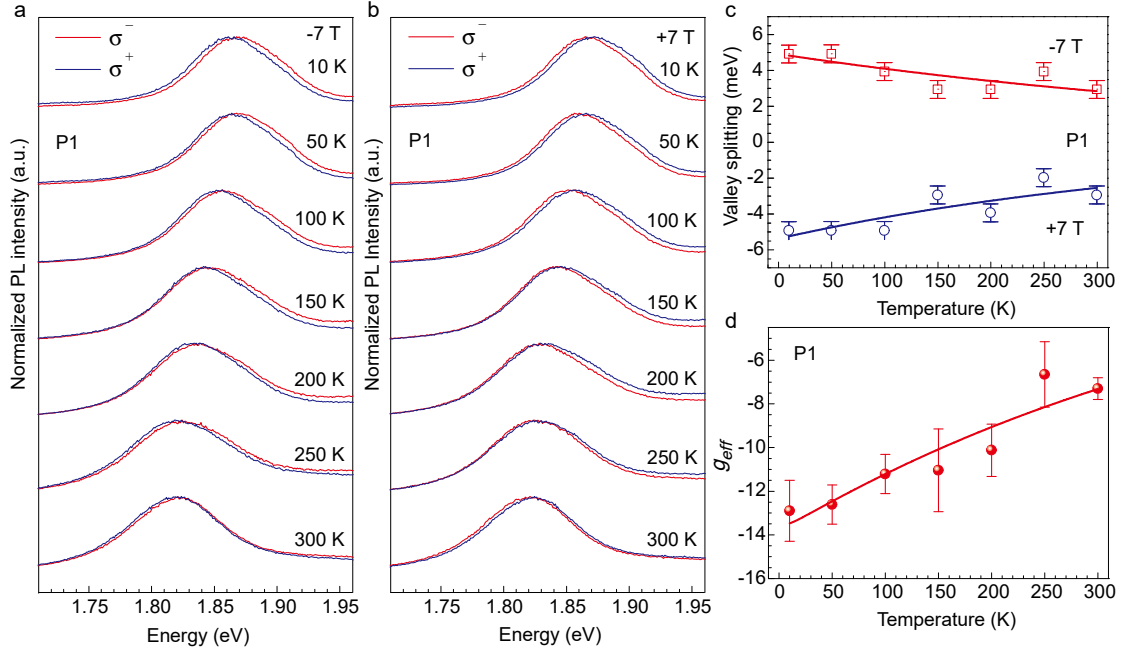


Figure 4. Temperature dependence of valley Zeeman splitting. (a, b) Normalized raw polarization-resolved PL spectra of the Fe-doped MoS₂ monolayer (P1, Fig. 1a) under a -7 T (a) and +7 T (b) magnetic field as a function of temperature. (c, d) Valley Zeeman splitting (c) and g_{eff} factor (d) as a function of temperature. The solid lines are fits to the data obtained using the temperature dependence of the exchange constant of isotropic Heisenberg exchange interaction mode, as described in the text.

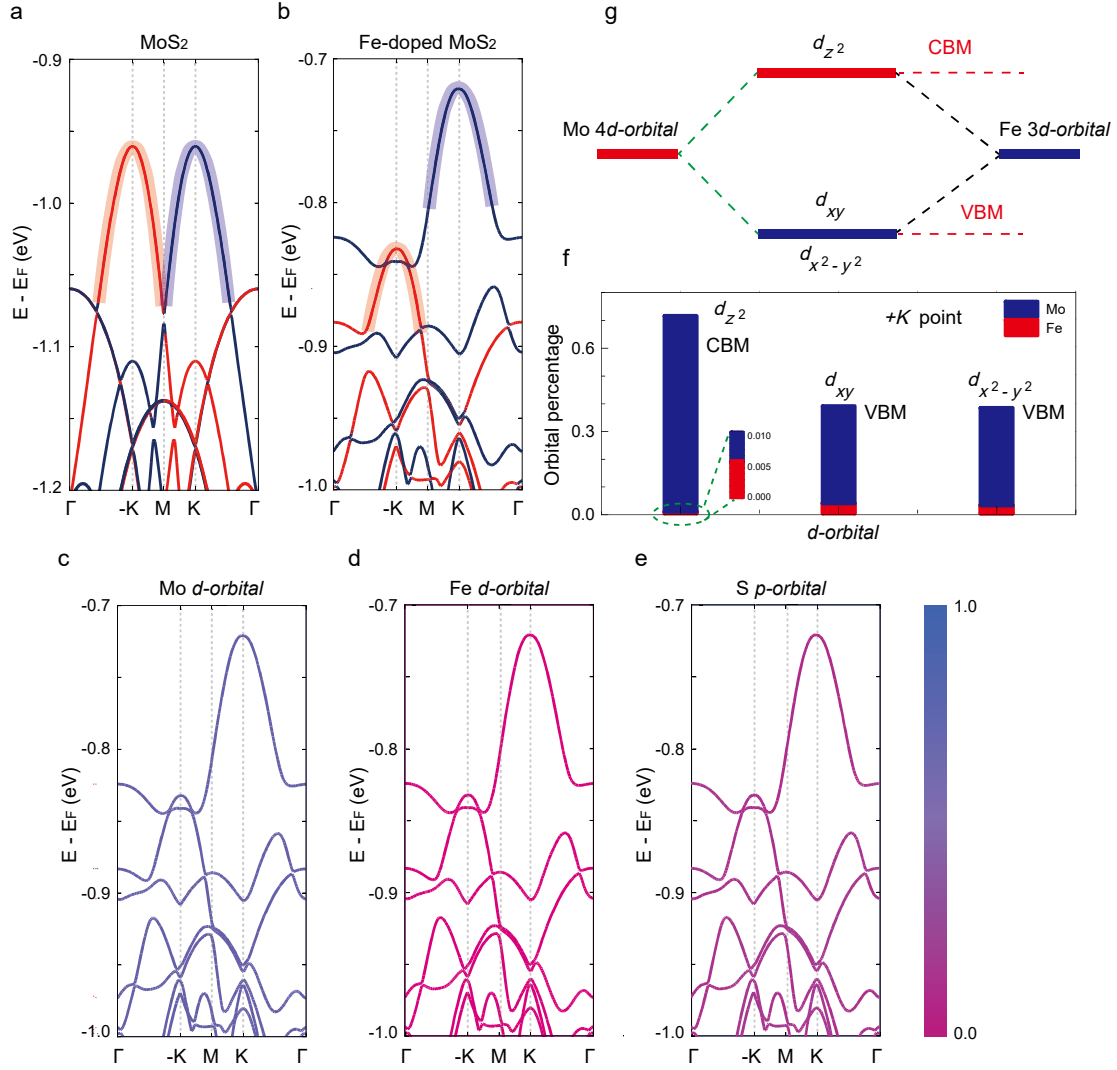


Figure 5. Origin of valley Zeeman splitting in Fe-doped monolayer MoS₂. (a) Electronic band structures of undoped monolayer MoS₂ with SOC, exhibiting an emerging valley pseudospin. (b) Electronic band structures of Fe-doped monolayer MoS₂ with SOC and the exchange field, demonstrating valley Zeeman splitting. Blue (red) curves represent spin up (down) states in the +K (-K) valley. (c-e) Corresponding electronic band structures of the d -orbitals and p -orbitals of Mo, Fe and S atoms in Fe-doped monolayer MoS₂. The colorbar represents the percentage that each set of orbitals contributes to the overall valence band. (f) Corresponding every isolator d -orbital percentage in the hybridized d -orbitals of the Fe-doped

monolayer MoS₂. The VBM mainly consists of the $d_{x^2-y^2}$ and d_{xy} orbitals of Mo and Fe, while the CBM comprises the d_{z^2} orbitals. The Fe d -orbitals unambiguously contribute to the orbital hybridization, although their fractions are tiny as compared to Mo d -orbitals. (g) Schematic of the d -orbital hybridization of Fe and Mo atoms. All the above calculated results are from a 5×5 MoS₂ supercell with one Fe atom instead of one Mo atom. The valley Zeeman splitting between the $+K$ and $-K$ valleys mainly originate from the valance band shifts (Fig. S11b-c), thus only the valance band structures were shown here.

TOC:

